# High-Resolution Daytime Cloud Observations for Northwestern Mexico from *GOES-7* Satellite Observations

JAIME GARATUZA-PAYAN

*Department of Hydrology and Water Resources, The University of Arizona, Tucson, Arizona*

RACHEL T. PINKER

*Department of Meteorology, University at Maryland at College Park, College Park, Maryland*

W. JAMES SHUTTLEWORTH

*Department of Hydrology and Water Resources, The University of Arizona, Tucson, Arizona*

(Manuscript received 8 June 1999, in final form 9 February 2000)

ABSTRACT

The first stage in a program of research to develop a regional model capable of describing the hydrology of semiarid areas of northwest Mexico and southwest United States, using remotely sensed data, is described in this paper. Finescale information on cloud cover is required to provide the radiation forcing for making simple, near-real-time estimates of daytime evaporation in hydrologic models, and frequent satellite observations have the potential to document cloud variability at high spatial and temporal resolutions. In this study, the operational framework for obtaining information on cloud cover was developed and applied, using hourly sampled, 1-km resolution *GOES-7* data as received in real time in Obregon, Mexico. These satellite data were collected and analyzed from 1 July 1993 to 31 July 1994 for an approximately $10^6$ km$^2$ rectangular area in northwest Mexico. An efficient method was devised to provide clear-sky radiance images for the study area, at 4 km $\times$ 4 km resolution, and updated at monthly intervals, by applying thresholds indexed to the locally appropriate clear-sky radiance, thereby allowing for spatial and temporal changes in surface conditions. Manual image inspection and comparison with ground-based measurements of cloud cover and surface solar radiation provided reassurance that the high-resolution cloud-screening algorithm gave satisfactory results.

This algorithm was applied to investigate the effects of temporal sampling frequency on estimates of daytime-average cloud cover and to document aspects of the cloud characteristics for the study area. The high-resolution algorithm proved to be efficient and reliable and bodes well for its future use in providing high-resolution estimates of surface solar radiation for use in a hydrologic model. Monthly clear-sky composite images were consistently generated, showing little evidence of contamination by persistent clouds, and tracked the seasonal evolution in surface radiance. Comparison with ground-based measurements gave confidence in the credibility of the satellite estimates and revealed weaknesses in the Campbell–Stokes solarimeter. The seasonal evolution of spatial patterns of cloud and its diurnal cycle were investigated. The average cloudiness for the study area is 0.25, with a substantial annual variation from 0.19 in April to 0.40 in December. Persistent cloudy conditions throughout the year were detected over the Pacific Ocean west of Baja California. The derived high-resolution cloud estimates, when compared with similar estimates from the International Satellite Cloud Climatology Project (ISCCP D1), were about half those obtained with the low-resolution data, indicating that, in this complex study area where land and water boundaries are in close proximity, low-resolution satellite observations of clouds may not be able to depict the true cloud cover.

## 1. Introduction

The radiation balance at the top of the atmosphere and that at the earth's surface provides a fundamental constraint on climate (Pexioto and Oort 1992), and clouds are the major control of the difference between these two. Clouds also provide the primary link between the two surface energy exchange processes that influence climate, namely, the exchange of shortwave and longwave radiation and the exchange of water.

Until recently, surface observations of the extent and nature of cloud cover have served as the major source of information on clouds (Warren et al. 1986), and past estimates of the radiative effects of clouds were based on such surface observations (House et al. 1986). However, surface observations are rare over oceans and un-

*Corresponding author address:* Prof. W. James Shuttleworth, Department of Hydrology and Water Resources, The University of Arizona, Harshbarger Building 11, Tucson, AZ 85721-0011.
E-mail: shuttle@hwr.arizona.edu

populated land areas, and they are only point samples that provide little information on the spatial variability of clouds. Numerous studies have explored the microphysics and dynamics of clouds at the scale of individual cloud elements (e.g., Pruppacher and Klett 1980; Cotton and Anthes 1989; Minnis and Smith 1998; Lin et al. 1998a,b; Minnis et al. 1993; King et al. 1996). Measurements of the extent and of optical properties of clouds using earth satellites have the potential to supplement surface observations and in situ studies by extending measurements to larger time- and space scales and by providing information on cloud radiative properties. This prospect motivated the International Satellite Cloud Climatology Project (ISCCP), which was established by the World Climate Research Program (WCRP) in 1982 to collect and analyze satellite radiance data and, from this, to produce a uniform global cloud climatology (Schiffer and Rossow 1983; Rossow and Schiffer 1991).

Estimates of the effect of clouds on radiation made during the Earth Radiation Budget Experiment (Harrison et al. 1990; Kandel and Fouquart 1992; Wielicki et al. 1995) and numerical experiments using general circulation models (GCMs) have demonstrated the important role of clouds in determining potential climate change (Cess et al. 1990; Gleckler et al. 1995). GCM experiments show that an evolving climate system may involve changes in cloud fraction, cloud height, and/or cloud optical depth. Because of the great disparity between the spatial scale of cloud convective processes (typically 100 m to a few kilometers) and GCM grid boxes (typically a few hundred kilometers), accurate modeling of cloud processes in global climate models is likely to remain a long-term challenge. Meanwhile, satellite-derived cloud information offers an opportunity to both monitor the earth's climate system and to test the validity of GCMs. The focus of interest in this study was to derive satellite-based estimates of fractional cloud cover at high spatial resolution over an area of about $10^6$ km$^2$ in a semiarid region of northwest Mexico during daylight hours, when most of the evaporation takes place.

Regional or global observations of cloud cover allow better understanding of how cloud characteristics are associated with different climatic and dynamic regimes in the atmosphere (Stowe et al. 1988; Rossow et al. 1989a). Meteorological satellites allow quasi-continuous cloud observations over the whole globe, thus providing an opportunity to study the behavior of clouds on time- and space scales that are not accessible using in situ and aircraft data. Satellites can observe cloud variations from about 100 m to planetary scales and from about 15 min to several years. Satellite-based cloud analyses are motivated primarily by a desire to learn how variations in clouds affect the radiation balance. The relationship is not simple because cloud optical properties can change quickly and over relatively small distances. Moreover, clear-sky brightness (used to establish thresholds for cloud detection) varies as a function of time, space, and view angles, and it can be difficult to establish thresholds for detecting the presence of clouds under all circumstances, using only one visible imagery channel and an appropriate single-channel cloud classification scheme. Thus, the limitations of available satellite data preclude the measurement of all the important properties of clouds. Nonetheless, it is assumed that cloud amount, cloud-top temperature, and optical thickness, the cloud properties that affect satellite-measured radiance (Rossow and Garder 1993) are also the properties that most affect the total radiation balance. To maintain physical consistency, radiative transfer models are used to relate cloud properties both to satellite-measured radiance and to the complete radiation balance.

Previous satellite-based studies of clouds have examined the mean properties of clouds, their regional and seasonal variations (Stowe et al. 1988; Rossow et al. 1989a,b; Wylie and Menzel 1989), and some aspects of their long-term variability (Short and Cahalan 1983). However, there have been few systematic studies of cloud variability at small spatial scales and high temporal resolution, and even fewer attempts to evaluate such estimates. In the present study, the cloud detection method originally developed by the National Oceanic and Atmospheric Administration's National Environmental Satellite Data and Information Service (NOAA/NESDIS) in support of the Global Energy and Water Cycle Experiment's (GEWEX) Continental-scale International Project (Leese 1994, 1997) has been modified. The NOAA/NESDIS detection methods were developed to facilitate the production of real-time estimates of surface and top-of-the-atmosphere radiative fluxes over the United States at hourly intervals and 0.5° spatial resolution from GOES data (Tarpley et al. 1996). Two channels of *GOES-8* data are first reduced to a common resolution of 4 km. These 4-km pixels are then classified as either clear or cloudy, and the fractional cloud cover is calculated for the 0.5° grid. This is then used to infer the radiation fluxes at the surface using the physical model described in Pinker and Laszlo (1992).

While multichannel cloud detection algorithms (e.g., the ISCCP detection method) might have an advantage over a single-channel algorithm, there is a trade-off in scale. The visible channel has higher spatial resolution (1 km in *GOES-7*) than the infrared channel (8 km in *GOES-7* but 4 km in *GOES-8, -9,* and *-10*). Therefore, if both channels were to be used, it would be necessary to reduce the resolution of the visible channel to the one of the infrared channel, hence compromising the resolution attainable from the visible channels and losing information at high spatial resolution.

In this study, the above-described approach was modified and applied to a relatively small region with a 1-km resolution in the visible channel of *GOES-7* to give cloud information that was obtained from processing at 1-km pixel level and subsequently mapping this infor-

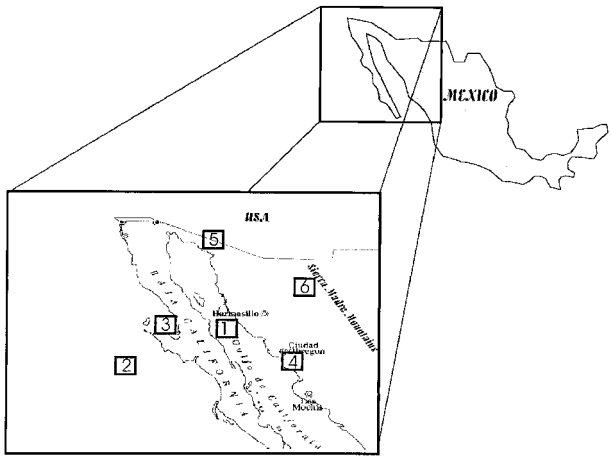


FIG. 1. Location of the study area with selected contiguous rectangular areas of approximately 20 km × 20 km (5 × 5 pixels) that are given focused attention in this study. These areas are selected to be representative of 1) the Gulf of California, 2) the Pacific Ocean, 3) the Vizcaino Bay, 4) an area with irrigated agriculture, 5) desert areas, and 6) the Sierra Madre Occidental.

mation onto a 4-km grid. To do this, an efficient procedure was developed to detect the presence of clouds using thresholds that allow for random noise and seasonal changes in the background clear-sky radiance. For evaluation purposes, this new high-resolution procedure was applied over an annual cycle to investigate the seasonal and diurnal variations of cloud cover in the study region, and the results were compared against visual satellite images and with other sources of cloud information. The implementation, application, and results of that evaluation are presented in this paper.

## 2. Study area

The study area is a 1024 km × 1024 km region (23°–32°N, 106°–117°W) in northwest Mexico that includes the states of Baja California, Sonora, Sinaloa, and part of Chihuahua (Fig. 1). This area has highly variable topography, with plains in the northwest and some elevated plateaus above 1500 m. It includes the Sierra Madre Occidental that have elevations typically greater than 3000 m and steep slopes, especially in the south where the mountains almost reach the coast.

The climate of this region is very dry. The dominant synoptic factor is a pressure belt associated with the ''Bermuda high,'' which lies south of Mexico in the winter and north of Mexico in the summer, implying westerly and easterly air flow in winter and summer, respectively. The continuous proximity of the high pressure (and the associated subsidence) result in relatively sparse cloud cover and little rain, especially in late spring, when the center of the high pressure belt is situated at about the same latitude as the study area. During the winter months (November–February), the region is intermittently influenced by polar disturbances that result in increased cloudiness and, in some cases, rainfall. From March to June, cloudiness decreases, and May and June are usually characterized by the absence of rain and low relative humidity. The temperature reaches its maximum in June, prior to the onset of the ''Mexican monsoon'' (Douglas et al. 1993), when there is a sharp increase in relative humidity and a slight decrease in daytime temperatures. In July, August, and September, local storms and tropical disturbances, either in the form of cyclones or mesoscale convective complexes, bring increased cloudiness and rain. Rainfall is then usually in the form of intense convective storms.

Rainfall in northwest Mexico during the months of July–September accounts for 60%–80% of the total annual rainfall (Douglas et al. 1993), with rainfall totals in some locations along the western slopes of the Sierra Madre Occidental exceeding 650 mm during this 3-month period. Mean monthly total rainfall exceeds 300 mm at many locations. Average yearly precipitation is around 350 mm, but it ranges from less than 200 mm at the coast to approximately 400 mm at the foot of the Sierra Madre Occidental, and up to 800 mm at higher elevations in these same mountains. Average daily temperature varies from 18°C in January to 31°C in July, and the daily temperature range is typically 10°–15°C. Average daily relative humidity ranges from 70% in the two wet seasons to 50% in May and June, when daytime relative humidity can be 25% or less.

## 3. Observations and methods

### *a. Satellite data*

The primary observations collected for this study are the reflected visible (0.52–0.72 $\mu$m) and emitted infrared (10.5–12.5 $\mu$m) radiances observed by the imaging visible-infrared spin-scan radiometer on the *GOES-7* satellite. Twelve visible images (hourly, for daylight hours) and 24 infrared images (hourly, for the whole day) were collected daily from 1 July 1993 to 31 July 1994 by a GOES receiving station located at the Instituto Tecnológico de Sonora (ITSON) in Obregon, Mexico. Only the visible images were used in this study. To a large extent, the size of the individual picture elements (pixels) determines the spatial resolution of the satellite sensor. The *GOES-7* satellite viewed half of the earth in a single scene and provided visible data that had a stable, nonlinear response, 6-bit precision, and with the near-nadir view pertinent to the study site, at an approximate 1-km resolution.

The data used are full-resolution *GOES-7* images in raw data format, that is, in the form of dimensionless quantities that are proportional to the square root of the observed radiant intensity in the selected spectral band. The data were calibrated following the equation:

$$R = gc^2 - d, \quad (1)$$

where $R$ is the calibrated radiance (in W $m^{-2}$), $g$ ($=0.1624$ W $m^{-2}$) is the gain coefficient, $c$ is the raw data value, and $d$ is the ''deep space'' radiance (2 W $m^{-2}$). In this equation, the values of $g$ and $d$ are taken from Whitlock et al. (1990), but they are converted for use with 6-bit (rather than 8-bit) data.

The *GOES-7* data are prone to both systematic and nonsystematic geometric errors. These fall into two classes, namely, those that can be corrected using knowledge of platform ephemeris and internal sensor distortion, and those that cannot be so corrected with acceptable accuracy without a sufficient number of ground control points. Documentation of ephemeris was provided operationally along with the satellite data received in real time at ITSON. A two-step process was used to coregister all the images to a standard image in which each pixel corresponds to the same place on the earth's surface. This two-step process comprised an automatic geometric correction (using the ephemeris data) that was made as soon as the image was received, followed by a manual coregistration to provide a standard image at the end of each day. In this study, images were received and used every hour; geometric correction with ground control points was not attempted. Once the cloud cover analysis has been completed, the final product was geometrically corrected and transformed into the required map projection, using an algorithm that converted scan line and pixel coordinates into latitude and longitude.

### *b. Methodology*

Many authors have described the use of satellite data to determine cloud cover (e.g., Stowe et al. 1988; Warren et al. 1986; Wylie and Menzel 1989; Sèze and Rossow 1991). The earliest attempts used data from polar-orbiting satellites and were limited to one daylight image per day, which precluded investigation of diurnal changes in cloud cover. More recent research has used data from geostationary satellites that have better temporal resolution and that can therefore be used to assess variations in cloud cover.

When displayed in the form of histograms, the frequency distribution of the pixel radiance in a satellite image forms a continuum between ''clear'' values and ''cloudy'' values at all time- and space scales (Wielicki and Parker 1992). Fundamentally, cloud detection involves partitioning these radiance samples into three groups: one that has a high probability of being completely covered with clouds, one that is totally cloud free, and one that is partly covered by clouds. The decision rules used to discriminate between these groups are threshold statements. Thus, an individual pixel will be designated to be cloudy if the radiance is greater than a threshold value (e.g., 35% reflectance). Alternatively, it may be designated to be clear if the radiance is less than a pixel-specific, prescribed value (commonly set to be the inferred clear-sky value plus the estimated uncertainty in that clear-sky value). Pixels that are neither cloud covered nor clear are designated as ''mixed.'' The use of this approach minimizes false cloud detection, but it can miss light cloud if its measured radiance closely resembles that for pixels with no cloud.

In general, examination of the time records of visible radiance for a particular area reveals four types of variation (Sèze and Rossow 1991). In decreasing order of magnitude, these are

1) variations due to the formation/dissipation of clouds or movement of clouds,
2) periodic variations associated with changes in the solar illumination,
3) variations in surface conditions at synoptic and seasonal timescales, and
4) variations in radiance associated with changing atmospheric conditions.

The daily variation in solar illumination usually causes changes in surface radiance that are comparable with those caused by changing cloud cover. Success of the threshold method relies on accurately selecting the clear-sky threshold and, in this study, substantial effort centered on the development of a time- and space-dependent threshold. The ensuing algorithm for cloud screening involves the following two steps discussed below.

#### 1) DERIVING CLEAR-SKY COMPOSITE IMAGES

The radiance for each individual pixel was first corrected for changes in the sun-to-earth distance and the solar zenith angle (using standard equations and parameters from the Nautical Almanac). The full-resolution (1 km) pixels were then grouped into 4 km $\times$ 4 km ''target areas,'' and the average and standard deviations of the radiance were computed for each target area for each hourly image.

Variations in the clear-sky reflectance are usually smaller in time than in space. The generally small variations of surface reflectance in the visible wave band and the tendency for the surface reflectance to be smaller than cloud reflectance produce a characteristic shape in the darker part of the visible radiance probability distribution that is only weakly related to the surface cover (Sèze and Rossow 1991). This behavior of visible radiance (Reynolds and Vonder Haar 1977) allows the use of a simple statistic, namely, the minimum visible radiance, to estimate clear-sky values. In a set period (in this study, selected to be 1 month), the satellite should measure the lowest radiance if there is no cloud present in the target area. The minimum measured radiance observed during any month can therefore be assumed to correspond to the radiance of the target area in clear-sky conditions and to provide a threshold that distinguishes cloudy from clear skies and that varies with location and also (in monthly steps) with time (Rossow and Garder 1993).

The procedure used to estimate the clear-sky reflectance for each target area, for each month, is illustrated

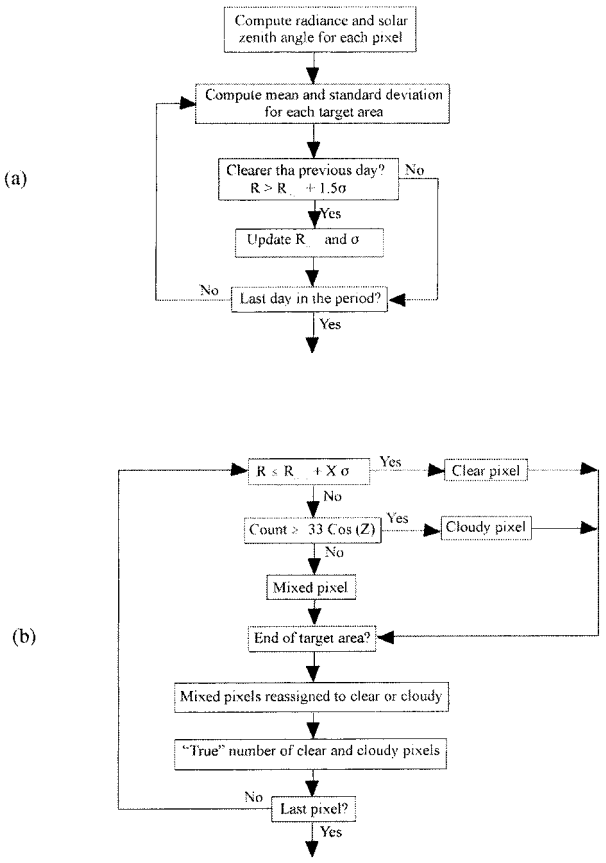


FIG. 2. (a) Flowchart of the process used to estimate the clear-sky reflectance for each of the 4 km × 4 km target areas in the monthly clear-sky composite images. (b) Flowchart of the processes used to assign pixels in each target area into the ''clear-sky'' and ''cloud-covered'' categories. [Note: In these flowcharts, $R$ is the actual radiance, $R_{clear}$ is the radiance for the relevant target area, $s$ is the variance of pixel radiance for the target area in the current image, $s_{clear}$ is the variance of pixel radiance in the target area in the clear-sky composite image, $Z$ is the solar zenith angle, and $X$ (=13) is the prescribed contrast threshold.]

in Fig. 2a. Corrections for satellite-viewing geometry were first applied for the angular dependence of clear-sky radiance for each individual pixel. A decision was then made as to whether to update the minimum value of radiance that (it was assumed) most reliably represents clear-sky conditions. The currently measured average radiance for each target area, $R$, replaced the previously stored minimum, $R_{clear}$, for the month, and the new standard deviation of radiance for the target area replaced the previously stored value:

$$s_{clear}, \quad \text{if } R < (R_{clear} + 1.5s_{clear}) \text{ and } s < 4s_{clear}.$$

This procedure was carried out for each of the 4 km × 4 km target areas in the image until the last day of each month, when the resulting minimum radiances were assembled into monthly ''clear-sky composite'' images.

#### 2) DERIVING FRACTIONAL CLOUD COVER

Specifying which pixels are cloud free involves comparing the measured radiance for the pixel [from Eq. (1)] with the radiance for the target area in which the pixel lies in the appropriate clear-sky composite image. The procedure is illustrated in Fig. 2b. Thus, the observed value of radiance for the pixel is compared against $R_{clear}$, the clear-sky composite value for the target area in which it falls and, if the observed value is less than $(R_{clear} + 13s_{clear})$, the pixel is classified as being a clear-sky pixel. The factor 13 is sometimes called the ''contrast threshold'' and may vary with application (NOAA/NESDIS, for instance, uses 9 for the contrast threshold in their 0.5° estimates). Typically, it represents a reflectance of about 10%. If the observed raw data count is greater than 33 times the cosine of the solar zenith angle, $Z$, the pixel is classified as being totally cloud covered (i.e., in raw data terms, the value 33 is radiance prescribed to bright cloud in this study). If the pixel does not fall into either the clear-sky or totally cloud-covered categories, it is classified as having mixed cloud cover.

Pixels defined as having mixed cloud cover were reallocated between the clear-sky and totally cloud-covered categories. The proportion of mixed pixels redesignated as clear-sky pixels is given by the ratio of the average measured radiance for mixed pixels minus the clear-sky radiance to the (prescribed) radiance corresponding to total cloud cover minus clear-sky radiance. The final step is to assign a fractional cloud cover to each target area on the basis of how many of the (16) contributing pixels have now been designated as having (complete) cloud cover.

## 4. Results and discussion

### *a. Clear-sky composite radiance images*

The frequency distribution of observed radiance in the clear-sky composite images for the study area for each month between July 1993 and July 1994 is shown in Fig. 3. In these diagrams, the differing radiance of water and land is clearly visible: the narrower peak at lower values corresponds to water surfaces, while the broader peak at higher radiance corresponds to land surfaces. Figure 3 shows that the range of radiance values present in the image changes with season, being largest from December to March and less at other times. The mean values of radiance for water and land also change gradually throughout the year, as noted by Sèze and Rossow (1991).

As explained earlier, when specifying the cloud cover for a particular target area, the primary concern is to avoid introducing a bias in the clear-sky radiance in regions where time variations are greatest and to minimize any contamination that may result from the presence of unusually persistent clouds. In Fig. 3, the two peaks for water and land surfaces are both reasonably

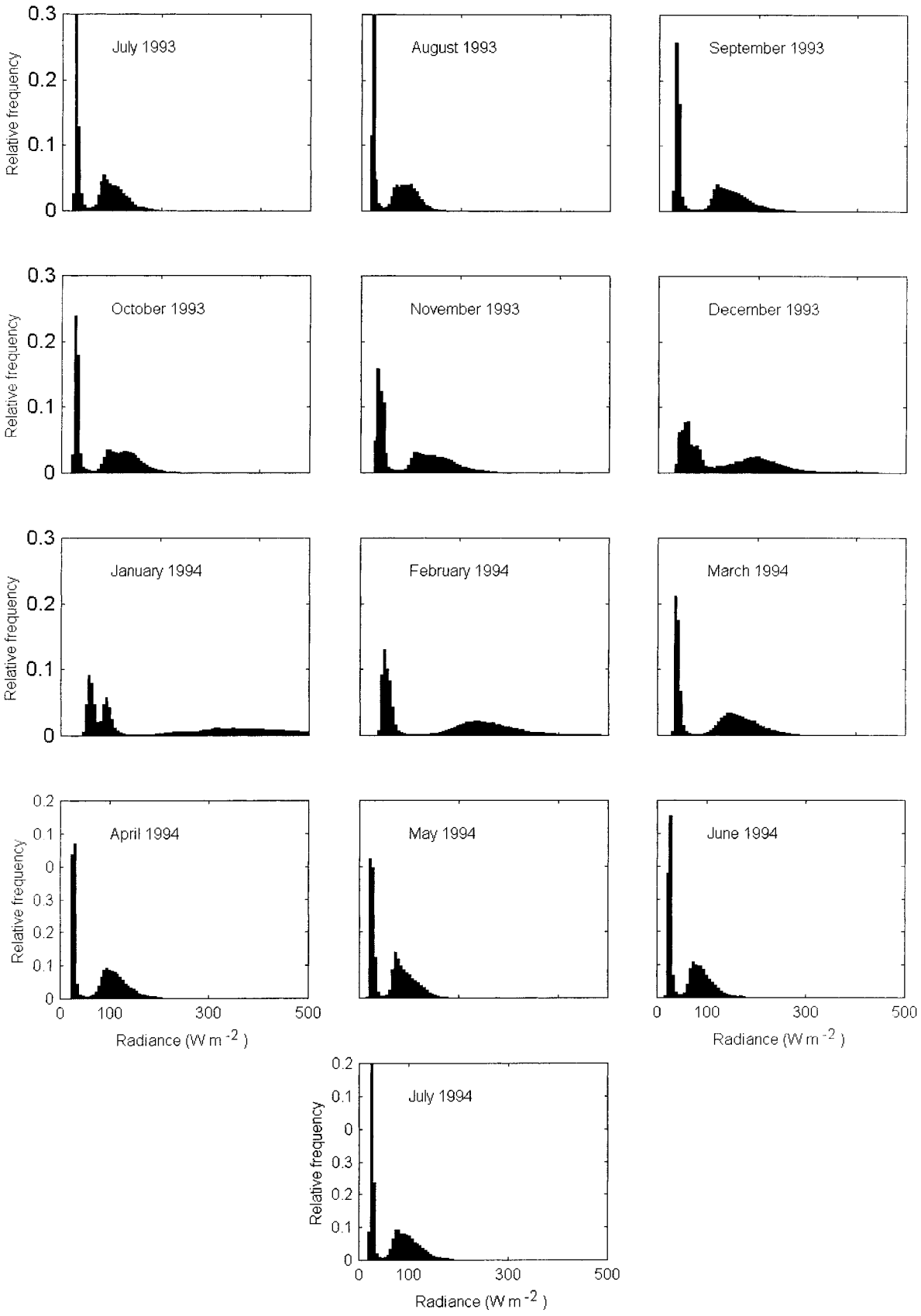

narrow and well-defined relative to the full range of radiance, indicating that changes in the frequency distribution from month to month are significant but not rapid. Moreover, there is no extended tail toward higher values of radiance in the frequency distributions. These facts suggest that, in this study area, some clear-sky conditions are always encountered for each target area when the clear-sky composite images are built over one month, and that there is little evidence of cloud contamination in the clear-sky composite image. Seasonal variations in surface radiance in the visible wave band for land surfaces are also visible in the monthly clear-sky composite images of the study area for July 1993 to July 1994 (Fig. 4). However, as might be expected from the clear separation between the peaks shown in Fig. 3, the water and land are always distinct.

The clear-sky composite images for the month of July in two consecutive years (1993 and 1994) shown in Fig. 4, and the equivalent frequency distributions given in Fig. 3, suggest that surface radiance does not change much from year to year. The (bimodal) frequency distributions in July 1993 and July 1994 have mean values of 67.7 and 63.1, respectively, and the mean values for the two modes (water and land) are 27 and 83 and 27 and 78, respectively. This is presumably because, in this study area, the seasonal evolution of surface vegetation is fairly consistent from one year to the next.

### *b. Comparison with ground observations*

For the duration of the study, ground-based estimates of fractional cloud cover were available from a Campbell–Stokes solarimeter located at the National Meteorological Service Observatory in Obregon, Sonora (27.36°N, 109.91°W). In addition, solar radiation data were collected using an Eppley pyranometer located at a site in the irrigated region around Obregon (27.36°N, 109.91°W). Figure 5a shows a comparison between satellite-derived estimates of daily average cloud cover and ground-based estimates given by the Campbell–Stokes solarimeter at the National Meteorological Service Observatory. It is important to recognize that the ground-based measurements are made at a single point, while the satellite estimate is a spatial average over approximately 16 km$^2$. It is likely that most of the random discrepancies in Fig. 5a are due to this sampling difference, although variations in aerosol optical thickness or in the amount of ozone or water vapor concentration in the atmosphere could also contribute. The regression coefficient between the two estimates for the 13 months for which daily values are available is 0.81.

In Fig. 5a, a systematic error in the measurements made with the Campbell–Stokes instrument is revealed. Early in the morning and late in the afternoon, this instrument tends to underestimate sunshine hours because the sun lacks sufficient intensity to burn the paper chart, this being the basis of the measurement. A detailed inspection of the burnt charts for totally clear days and comparing the resulting estimate of sunshine hours with the day length given in astronomical tables suggested that the Campbell–Stokes instrument is reliable for approximately 1 h less than the actual day length. Figure 5b shows a second comparison between the Campbell–Stokes and satellite estimates of cloud cover. In this figure, the estimated cloud cover is the daily average value for the period starting 30 min after dawn and ending 30 min before dusk in each case. In this figure, there is an obvious and significant improvement in the quality of the comparison between the two estimates, especially at low values of cloud cover.

In Fig. 6, the relationship between the daily average solar radiation measured by the Eppley radiometer normalized by extraterrestrial solar irradiance (Iqbal 1983) as a function of the satellite estimate of daily average fractional cloud cover is shown for the target area centered on site of the Eppley radiometer. The effect of sampling differences between the ground-based instrument and the satellite-based area-average estimate is again apparent in this figure. Notwithstanding these random discrepancies, the approximately linear relationship between observed surface radiation and satellite-derived cloud cover shown in Fig. 6 (and that found in similar plots for individual months not shown) provides reassurance that the finescale cloud-screening algorithm is reasonably effective in operation. The line shown in Fig. 6 corresponds to the Brunt equation:

$$S_t = [a_s + b_s(n/N)]S_o, \tag{2}$$

where $S_t$ is the estimated solar radiation, $S_o$ is the extraterrestrial solar irradiance, $n$ is the number of bright sunshine hours per day, $N$ is the total day length, $a_s$ is the fraction of extraterrestrial radiation measured at the ground on totally overcast days ($n = 0$), and $(a_s + b_s)$ is the fraction of extraterrestrial radiation measured at the ground on totally clear days ($n = N$). In this equation, the daily average cloud fraction corresponds to $(1 - n/N)$. A linear regression analysis between normalized solar radiation and satellite-derived estimates of cloud cover gave the values $a_s = 0.27$ and $b_s = 0.68$ for the Angstrom coefficients in Eq. (2), with a regression coefficient of 0.7. These values are plausible in comparison with typical values given in the literature (e.g., Shuttleworth 1993).

### *c. Cloud-cover environment of the study area*

Figure 7 shows average cloud cover for each month. In this figure, the coastline is always apparent because

←

FIG. 3. Histograms of the frequency of occurrence of radiance values in the monthly clear-sky composite images for the study area.

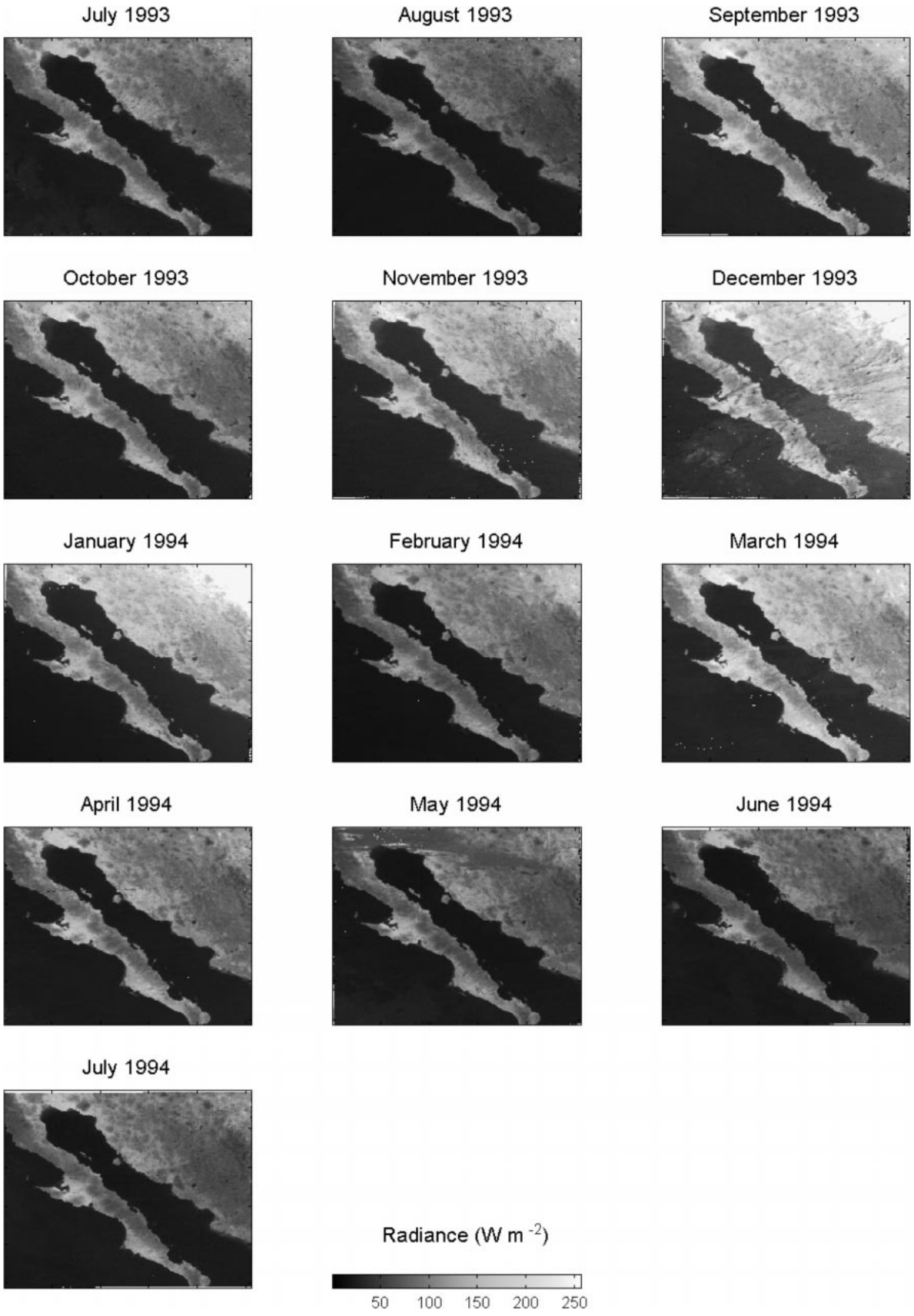

the cloud-retrieval algorithm takes into account the spatial variability in surface radiance. Water and land surfaces mix along the coast, resulting in high spatial variability. The result is high values of $s_{clear}$, and the coastal pixels are wrongly classified as having mixed cloud cover. In effect, the algorithm artificially generates narrow bands of mixed cloud along coastlines.

The average monthly daytime cloudiness is given in Table 1 for the six selected subareas corresponding to contiguous rectangular areas of approximately 20 km × 20 km (5 × 5 pixels) whose location is illustrated in Fig. 1. The observed cloudiness for the six selected areas is also shown in Fig. 8. Water surfaces and land surfaces are shown in the upper and lower parts of this figure, respectively.

The average cloudiness for the study area during the period July 1993–June 1994 is 0.25, but there is a substantial annual variation from 0.19 in April to 0.40 in December. The spring to summer dichotomy is apparent in the average values for the two seasons (0.19 in spring and 0.28 in summer). Figure 8 and Table 1 show that there are noticeable differences in cloudiness of the six selected subareas within the study region. In general, areas in the Pacific (the ocean area and Vizcaino Bay) have more clouds than the other regions, although the cloud amount in these areas is variable. There is significantly less cloud cover in the Gulf of California than for other water surfaces, and the cloud cover in this region has noticeable seasonal changes, with more clouds in winter and less (the least of all subareas) clouds during the dry season in April, May, and June. The desert region has consistently low cloud cover, but there is an increase during the monsoon season in July and August. The Sierra Madre Occidental generally have more clouds. The cloud cover over the (low lying) irrigated areas tends to be intermediate between that over the Sierra Madre Occidental range and that in the Gulf of California, and it exhibits some seasonal change linked to both the winter and summer (monsoon) rainy seasons.

Thus, the satellite-derived monthly cloud distributions observed during this study can be summarized as follows. Cloudy conditions persist throughout the year over the Pacific Ocean west of Baja California, with most clouds occurring in the summer over Vizcaino Bay (presumably associated with eastward convergence west of the Baja California barrier). There are less clouds over the region as a whole during spring (March–May) and, in most months of the year, over the Gulf of California and the Altar Desert. This is consistent with the recorded rainfall being less than 200 mm year$^{-1}$ over these areas. There are marked differences between spring (March–April) and summer (July–August) associated with the North American monsoon. Summer is the cloudy season. In the morning, convective clouds begin to develop over the Sierra Madre Occidental and over Baja California that disperse in the late afternoon, presumably after it rains. In spring, the dry air is almost cloud free, especially over the coastal plain. During the winter, the study area has comparatively uniform cloud cover.

The six selected subareas illustrated in Fig. 1 also were used to represent the most characteristic surface covers in the study area to examine the diurnal variation of clouds. Figure 9 shows the mean diurnal variation of cloud cover over these six subareas for the whole year and for the two (monsoon and winter) rainy seasons. The upper portions of this figure correspond to water surfaces and the lower portions to land surfaces.

There is an evident daily cycle in cloud cover over the water surfaces during the winter season, with peaks in the morning and afternoon, and fewer clouds at noon. This cycle is less obvious over the land surfaces, but there is some suggestion of a similar pattern in the case of the Sierra Madre Occidental and the irrigated area. There is a tendency for clouds to decrease over the Gulf of California during the day in the monsoon season, but this tendency is reversed over the Pacific Ocean. Over the irrigated area and the desert area, cloud cover tends to decrease through the day, whereas it tends to increase over the Sierra Madre Occidental. Although there is no clear evidence of a significant daily cycle over any of the regions when the data are averaged over a full year, it is possible that there is some tendency toward increased clouds during the afternoon.

### *d. Temporal and spatial sampling studies*

The plausible behavior of the clear-sky radiance images, the level of agreement with ground data, and convincing description of the cloud environment for the area described in previous sections give confidence in the cloud analysis methods used in this study. In this section, we use our high temporal and spatial resolution analyses to explore the reliability of cloud analyses made with less-frequent data and at reduced spatial resolution.

#### 1) REDUCED SAMPLING FREQUENCY

Observations from polar-orbiting satellites have been used frequently to estimate daily cloud cover, solar irradiance, and evaporation (Sunada et al. 1990; Lagouarde 1991; Seguin and Itier 1983). With only one observation per day, polar-orbiting satellites have the drawback that such estimates cannot correctly capture the daily average cloudiness. Here, we assess the reliability of estimating daily average cloud amount from a single im-

←

FIG. 4. Monthly clear-sky composite images for the study area.

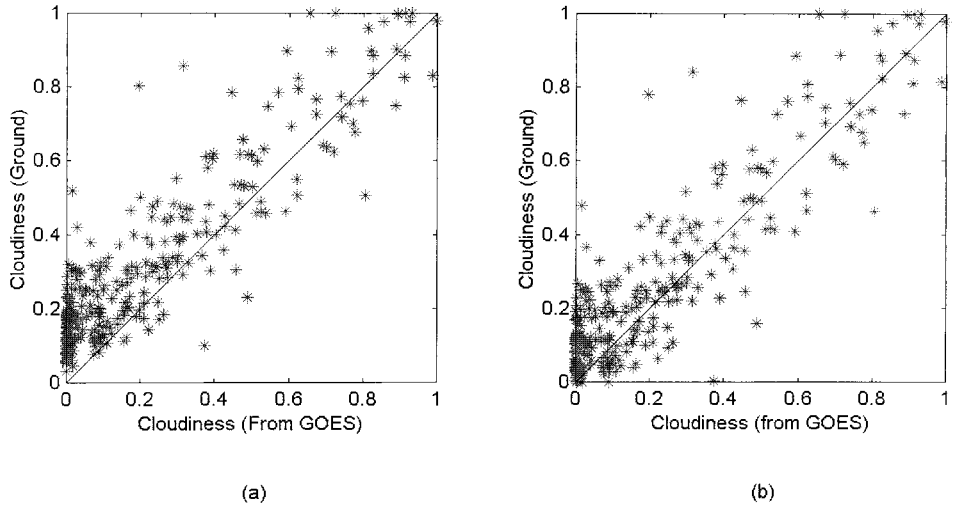


FIG. 5. The relationship between daily average cloudiness measured by a Campbell–Stokes solarimeter on the ground relative to that estimated from satellite data. (a) Values averaged over the full day length and (b) values averaged over the day length for which the Campbell–Stokes solarimeter is reliable.

age by comparing the cloud cover given by one observation at the time of overpass for polar-orbiting satellites (1000 LT in this region) with that derived from the 12-hourly observations available from geostationary satellites.

Figure 10 shows the comparison between the two estimates for the six subareas shown in Fig. 1 (i.e., areas representative of the Gulf of California, the Pacific Ocean, Vizcaino Bay, an area of irrigated agriculture, a desert area, and an area in the Sierra Madre Occidental). Table 2 gives the root-mean-square difference between the two estimates of daily average cloud cover for the six subareas in columns 2, 4, 6, 8, 10, and 12. The percentage of days for which the estimate from a single 1000 LT image is greater than that based on the average of 12-hourly images is given in columns 3, 5, 7, 9, 11, and 13. In general, if only one image were to be used to estimate the daily cloudiness, there would be an overestimation of the cloud cover for the Pacific Ocean and the Vizcaino Bay, and there would be an underestimation of cloud cover over the irrigated area and over the mountains. The error in estimated cloud cover would be greater for the Pacific Ocean and Vizcaino Bay and less for the desert area and the Gulf of California.

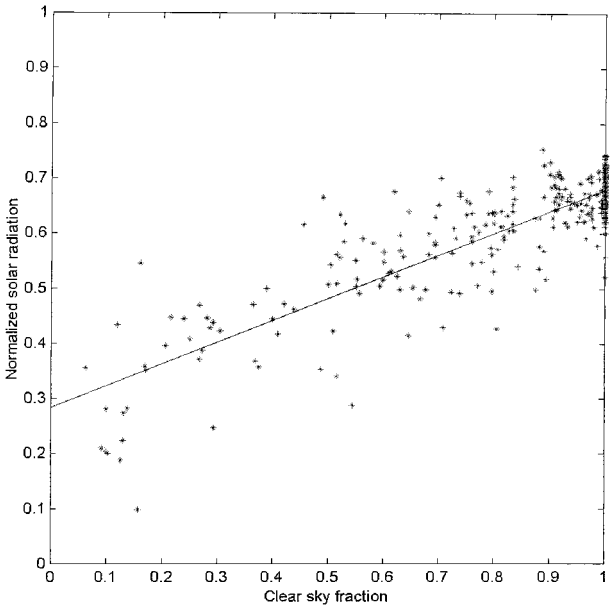


FIG. 6. Daily average solar radiation observed at the ground by an Eppley pyranometer normalized by extraterrestrial solar irradiance relative to the daily average cloud cover derived from satellite data. The regression line corresponds to Eq. (2) with Angstrom coefficients $a_s = 0.27$ and $b_s = 0.68$.

### 2) REDUCED SPATIAL RESOLUTION

The ISCCP was established as part of the WCRP in 1982 to collect and analyze satellite radiance measurements and to infer the global distribution of clouds, their properties, and their diurnal, seasonal, and interannual variations. The resulting data and analysis products have been widely used to improve the understanding and modeling of clouds and to improve understanding of the effects of clouds on the radiation balance. Data are being collected from both polar-orbiting and geostationary satellites and merged to provide gridded, global products that are archived at the Goddard Institute of Space Science. The ISCCP D1 product is currently the best source of low-resolution satellite-derived cloud information available. It is provided globally at 3-hourly intervals on an equal area grid with a resolution of 280 km.

A comparison was made over the study area between the satellite-derived (low resolution) cloud-cover estimates available in ISCCP D1 and the (high resolution)

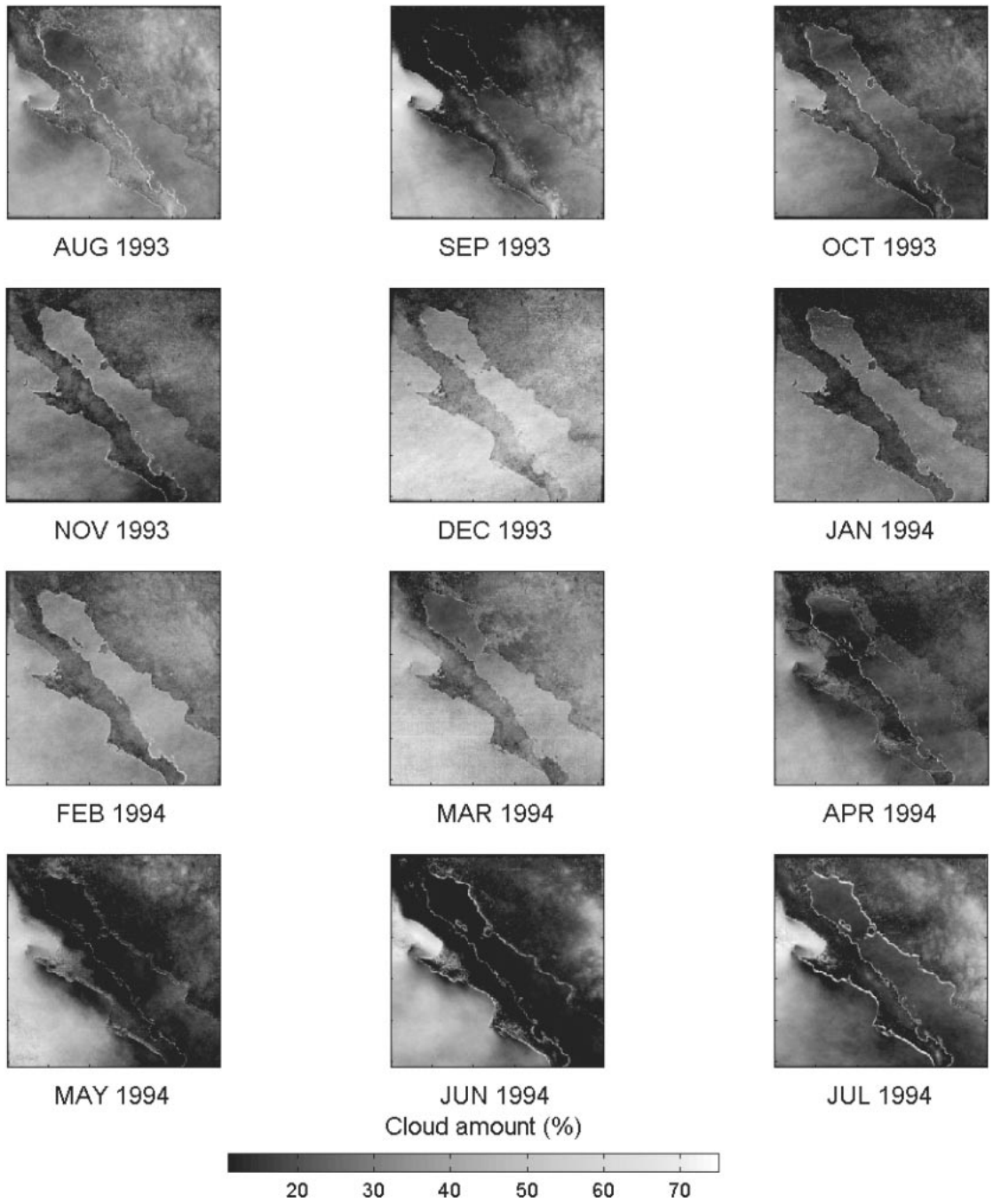


FIG. 7. Monthly average cloud cover images for one year for the study area.

cloud cover derived in this study. Figure 11 shows a comparison between daily average cloud cover given in ISCCP D1 and that derived in this study for two example months, August and October 1993. It is evident in Fig. 11 that, in this study region, a single ISCCP grid cell can span a region that includes different areas of water and land. The marked contrast between the reflectivity of water and land surfaces therefore complicates the specification of a threshold value that correctly identifies clouds in the grid box. The resulting error in the ISCCP dataset is most evident over the desert (site 5), which is well known for its very low cloud cover but where, in August 1993, a value greater than 60% is reported in the ISCCP data. Meanwhile, in Vizcaino Bay (site 3), a region known to have persistent clouds, the reported amount of cloud is much lower. In contrast, the high-resolution (4 km $\times$ 4 km) *GOES-7* estimate derived in this study mapped onto the ISCCP grid and

TABLE 1. Monthly average fractional cloud cover for daylight hours for the six subareas shown in Fig. 1 and described in the text and for the whole study area.

| Month | Gulf of California | Pacific Ocean | Vizcaino Bay | Irrigated agriculture | Desert | Mountains | Whole area |
|---|---|---|---|---|---|---|---|
| Jul 1993 | 0.020 | 0.572 | 0.364 | 0.248 | 0.196 | 0.363 | 0.273 |
| Aug 1993 | 0.164 | 0.403 | 0.349 | 0.274 | 0.221 | 0.375 | 0.288 |
| Sep 1993 | 0.037 | 0.429 | 0.484 | 0.268 | 0.059 | 0.211 | 0.216 |
| Oct 1993 | 0.153 | 0.289 | 0.381 | 0.171 | 0.130 | 0.208 | 0.189 |
| Nov 1993 | 0.313 | 0.315 | 0.306 | 0.184 | 0.106 | 0.231 | 0.212 |
| Dec 1993 | 0.325 | 0.590 | 0.443 | 0.403 | 0.128 | 0.336 | 0.404 |
| Jan 1994 | 0.178 | 0.282 | 0.246 | 0.162 | 0.078 | 0.136 | 0.196 |
| Feb 1994 | 0.301 | 0.348 | 0.362 | 0.233 | 0.166 | 0.299 | 0.281 |
| Mar 1994 | 0.155 | 0.461 | 0.413 | 0.268 | 0.136 | 0.284 | 0.309 |
| Apr 1994 | 0.104 | 0.381 | 0.316 | 0.203 | 0.216 | 0.132 | 0.186 |
| May 1994 | 0.034 | 0.428 | 0.434 | 0.084 | 0.243 | 0.185 | 0.194 |
| Jun 1994 | 0.057 | 0.368 | 0.579 | 0.111 | 0.188 | 0.195 | 0.203 |
| Jul 1994 | 0.143 | 0.216 | 0.612 | 0.177 | 0.273 | 0.307 | 0.443 |

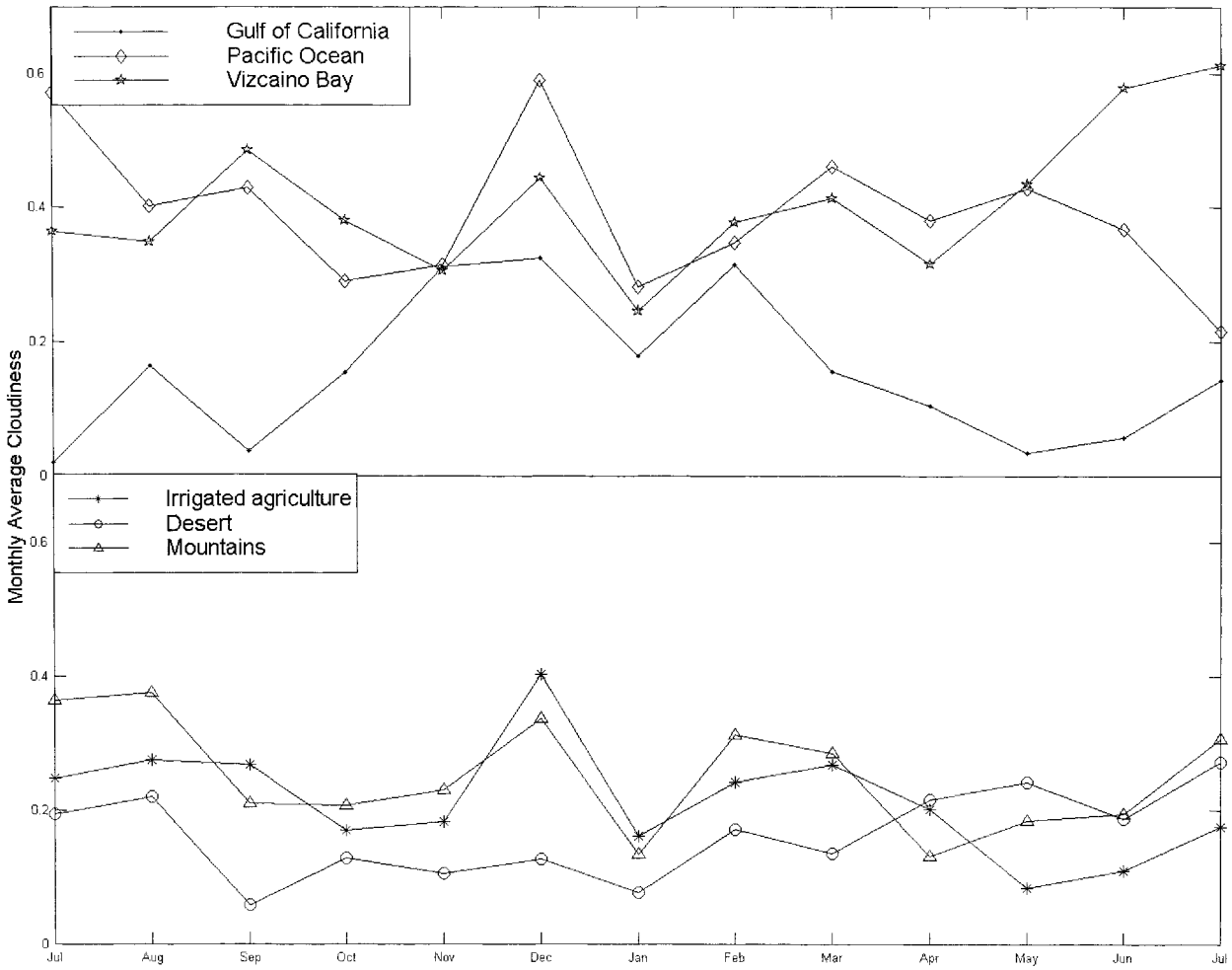


FIG. 8. The time dependence of monthly average fractional cloud cover for the six selected subareas shown in Fig. 1 and described in the text. The upper part of this diagram is for water (dots indicate data for the Gulf of California, diamonds for the Pacific Ocean, and pentagrams for the Vizcaino Bay). The lower part of the diagram is for land surfaces (asterisks indicate data for the area with irrigated agriculture, circles for the desert, and triangles for the mountains).

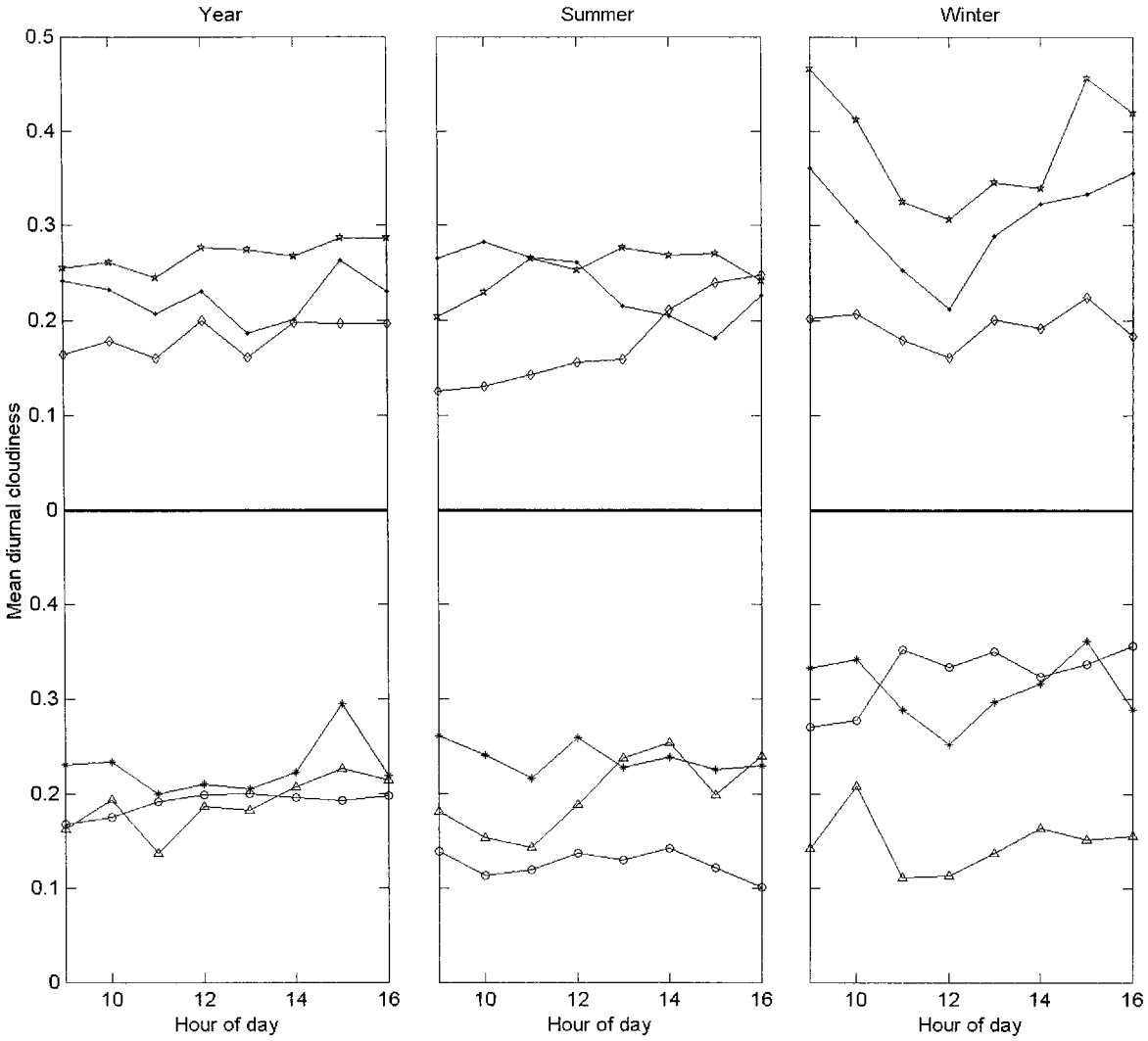


FIG. 9. Monthly average diurnal variation over the six selected subareas illustrated in Fig. 1 and discussed in the text for (a) the whole year, (b) the winter rainy season, and (c) the monsoon season. The upper part of this diagram is for water (dots indicate data for the Gulf of California, diamonds for the Pacific Ocean, and pentagrams for the Vizcaino Bay). The lower part of the diagram is for land surfaces (asterisks indicate data for the area with irrigated agriculture, circles for the desert, and triangles for the mountains).

averaged gave an estimated 20% cloud cover for the desert grid box and more than 60% for the Vizcaino Bay grid box during this month.

Table 3 gives the monthly average value and standard deviation of estimated cloud cover for the months of August to December 1993 given by ISSCP D1 and in this study. It is evident that, in this study region, where the underlying surface within an ISCCP data box is often a mixture of ocean and land, the low-resolution ISCCP data estimates of cloud cover are approximately twice those derived at high resolution from *GOES-7* data. However, both estimates have similar standard deviations. Perhaps this suggests that the discrepancies between the two estimates are due primarily to a difference in specifying the offset value used for clear-sky radiance at low and high spatial resolutions. To investigate the effect of difference in sampling procedure on the cloud amount, two months (June and July 1994) were analyzed in the same way as the ISCCP data, that is, only every eighth pixel was taken to form the input data to the cloud-screening algorithm. The results are given in Table 4, which shows that using reduced sampling results in higher cloudiness, thus suggesting that the ISCCP estimates of cloudiness are higher than our high-resolution estimates in this study region, not because the cloud screening used in deriving the ISCCP data detects more clouds, but as a result of sampling differences.

## 5. Summary and conclusions

The high-resolution (4 km) cloud-screening algorithm developed in this study proved to be efficient and re-

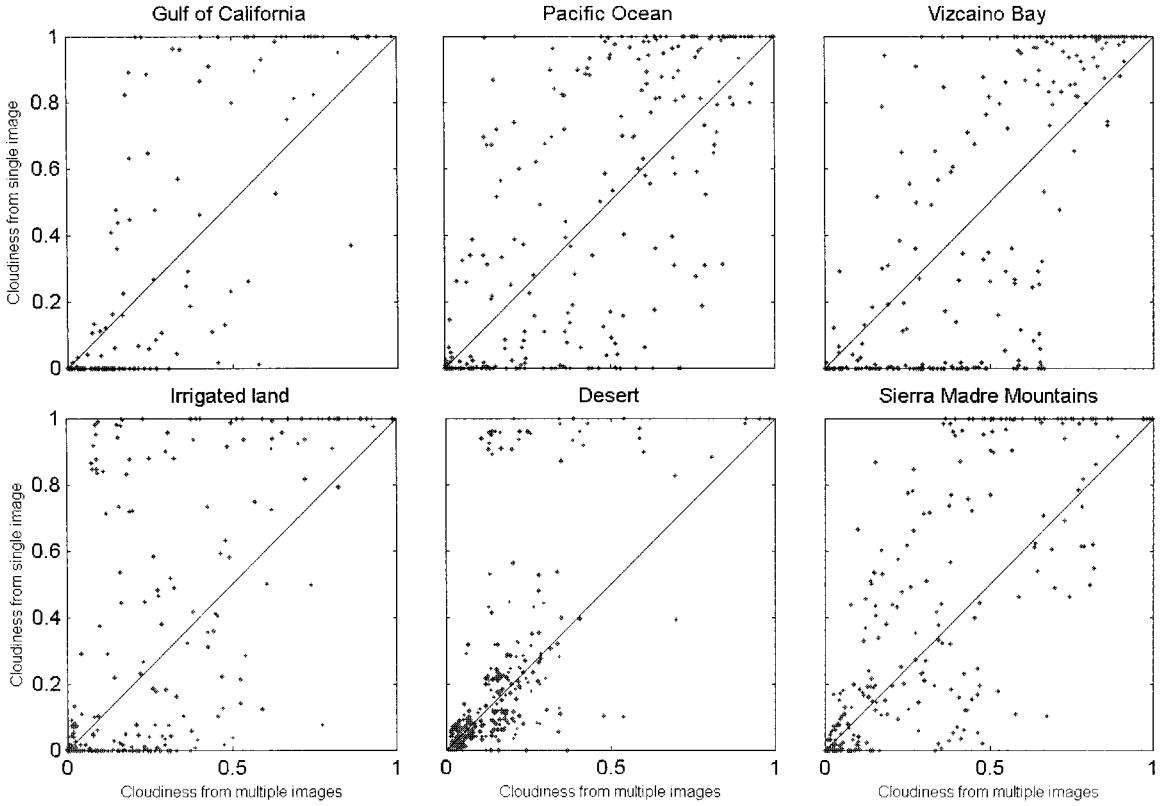


FIG. 10. Daily estimate of fractional cloud cover derived from the single (*GOES-7*) image at 1000 LT (to simulate the estimate that would be given by a polar-orbiting satellite for this study area) relative to that derived from the 12-hourly images from *GOES-7*.

liable when tested in application for 13 months for the selected study area in northwest Mexico. Monthly clear-sky composite images were consistently generated, which showed little evidence of contamination by persistent clouds and that tracked the seasonal evolution in surface radiance. These images were used to index the thresholds in a procedure that successfully classified the pixels in the 4 km × 4 km pixel target areas into clear-sky and cloud-covered categories.

Notwithstanding the difference in the nature of the sampling involved, comparison between the satellite-based estimates of cloud cover and ground-based estimates proved reassuring and, indeed, revealed weaknesses in the Campbell–Stokes solarimeter used to pro-

TABLE 2. The column headed ''rmse'' gives the root-mean-square error of the estimated cloudiness derived from a single image taken at 1000 UTC (to simulate a polar-orbiting satellite) relative to the daily average value estimated from the 12-hourly *GOES-7* images. The column headed ''% high'' gives the proportion of images (expressed as a percentage) for which the estimate of cloudiness derived from a single image taken at 1000 LT was higher than the daily average value from the 12-hourly *GOES-7* images. These results apply to the six selected subareas illustrated in Fig. 1 and described in the text.

| | Gulf of California | | Pacific Ocean | | Vizcaino Bay | | Irrigated land | | Desert | | Mountains | |
|---|---|---|---|---|---|---|---|---|---|---|---|---|
| Month | rmse | % high | rmse | % high | rmse | % high | rmse | % high | rmse | % high | rmse | % high |
| Jul 1993 | 0.042 | 52 | 0.278 | 76 | 0.364 | 84 | 0.302 | 28 | 0.097 | 0 | 0.206 | 36 |
| Aug 1993 | 0.219 | 59 | 0.284 | 55 | 0.371 | 72 | 0.242 | 34 | 0.168 | 28 | 0.253 | 28 |
| Sep 1993 | 0.084 | 59 | 0.263 | 81 | 0.345 | 78 | 0.194 | 26 | 0.047 | 15 | 0.186 | 48 |
| Oct 1993 | 0.257 | 52 | 0.306 | 76 | 0.256 | 60 | 0.193 | 32 | 0.113 | 40 | 0.160 | 32 |
| Nov 1993 | 0.221 | 55 | 0.244 | 55 | 0.321 | 45 | 0.204 | 23 | 0.119 | 27 | 0.151 | 27 |
| Dec 1993 | 0.151 | 69 | 0.181 | 92 | 0.267 | 92 | 0.264 | 77 | 0.127 | 92 | 0.083 | 31 |
| Jan 1994 | 0.163 | 42 | 0.271 | 50 | 0.234 | 62 | 0.181 | 42 | 0.084 | 62 | 0.228 | 35 |
| Feb 1994 | 0.286 | 48 | 0.273 | 52 | 0.224 | 52 | 0.201 | 26 | 0.196 | 91 | 0.243 | 35 |
| Mar 1994 | 0.125 | 53 | 0.267 | 76 | 0.313 | 71 | 0.246 | 53 | 0.094 | 12 | 0.221 | 24 |
| Apr 1994 | 0.359 | 47 | 0.317 | 74 | 0.411 | 68 | 0.217 | 21 | 0.383 | 84 | 0.306 | 32 |
| May 1994 | 0.056 | 33 | 0.289 | 87 | 0.286 | 80 | 0.114 | 33 | 0.187 | 33 | 0.164 | 40 |
| Jun 1994 | 0.113 | 21 | 0.294 | 68 | 0.391 | 89 | 0.158 | 21 | 0.113 | 71 | 0.265 | 14 |
| Jul 1994 | 0.181 | 59 | 0.310 | 62 | 0.335 | 86 | 0.248 | 31 | 0.106 | 72 | 0.247 | 24 |

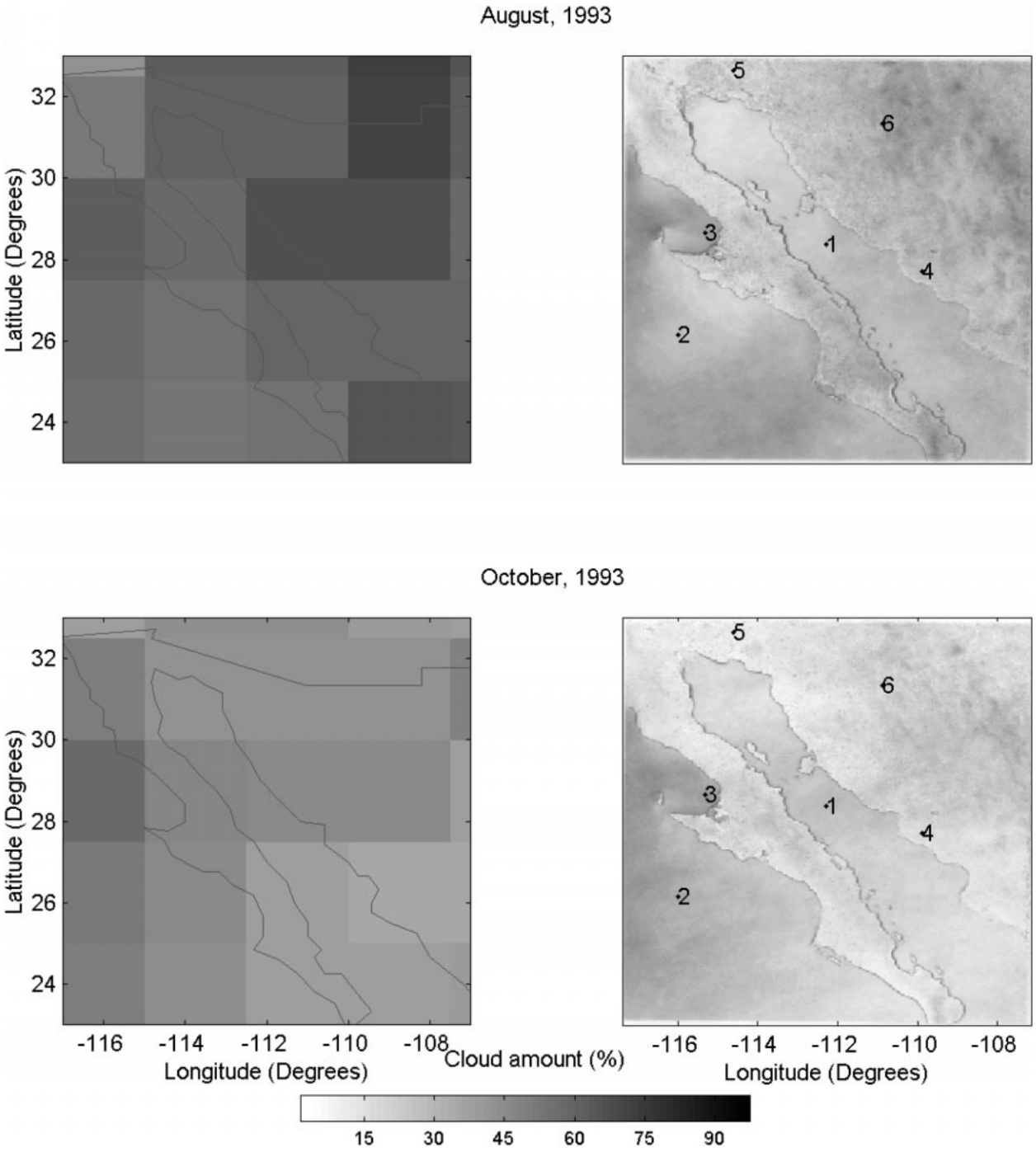


FIG. 11. Comparison between monthly average cloud amount for Aug and Oct 1993 taken from ISSCP D1 for 280 km × 280 km grid cells (to the left of the figure) and derived in this analysis from *GOES-7* data for 4 km × 4 km grid cells (to the right of the figure). The locations of the six selected subareas are also shown.

vide the ground-based estimates. Similarly, comparison with ground-based measurements of solar radiation gave confidence in the credibility of the satellite estimates of clouds.

The cloud-screening algorithm was used to explore the cloud-cover environment of the study area. The calculated monthly average values of cloud cover allowed the investigation of the seasonal evolution of spatial patterns of clouds and the diurnal cycle for selected areas of the study region and for the study region as a whole. The success of the high-resolution cloud-screening algorithm developed in this study bodes well for its

TABLE 3. Monthly mean and standard deviation (in brackets) of percentage cloud amount values for Aug–Dec 1993 from the ISCCP D1 dataset and derived at 4 km × 4 km resolution (from *GOES-7* data) in this analysis. The *GOES-7* data have been averaged for areas corresponding to the grid boxes in the ISCCP grid mesh that are closest to the six selected subareas shown in Fig. 1.

| Month (1993) | Site 1 | | Site 2 | | Site 3 | | Site 4 | | Site 5 | | Site 6 | |
|---|---|---|---|---|---|---|---|---|---|---|---|---|
| | ISCCP | *GOES-7* | ISCCP | *GOES-7* | ISCCP | *GOES-7* | ISCCP | *GOES-7* | ISCCP | *GOES-7* | ISCCP | *GOES-7* |
| Aug | 63.1 | 26.5 | 57.4 | 27.4 | 69.3 | 27.9 | 58.8 | 29.0 | 70.1 | 20.4 | 71.5 | 35.2 |
| | (25.2) | (26.2) | (27.1) | (25.6) | (19.9) | (20.9) | (21.1) | (24.8) | (26.8) | (15.3) | (21.7) | (21.6) |
| Sep | 49.2 | 15.2 | 58.7 | 35.0 | 51.2 | 23.5 | 63.2 | 19.6 | 38.9 | 2.6 | 36.6 | 16.0 |
| | (30.2) | (20.5) | (29.8) | (22.7) | (24.8) | (11.0) | (30.8) | (24.2) | (26.8) | (2.1) | (29.3) | (18.9) |
| Oct | 59.1 | 22.2 | 56.0 | 29.6 | 68.1 | 23.5 | 35.3 | 20.4 | 53.0 | 10.0 | 55.0 | 18.2 |
| | (31.6) | (25.3) | (36.5) | (29.0) | (22.2) | (21.4) | (29.4) | (24.3) | (27.7) | (14.8) | (26.4) | (19.4) |
| Nov | 58.9 | 30.7 | 55.4 | 32.2 | 68.3 | 27.1 | 47.9 | 26.4 | 55.9 | 12.3 | 49.0 | 20.5 |
| | (35.3) | (24.3) | (34.6) | (26.8) | (25.9) | (23.0) | (34.7) | (21.4) | (34.1) | (14.9) | (34.6) | (24.5) |
| Dec | 62.2 | 49.3 | 74.7 | 52.9 | 70.7 | 31.2 | 59.0 | 53.0 | 46.4 | 14.5 | 50.7 | 31.1 |
| | (38.3) | (31.6) | (30.6) | (32.2) | (27.6) | (32.4) | (30.6) | (29.3) | (32.8) | (21.7) | (36.4) | (33.4) |

future use in the application for which it was created, namely to provide high-resolution estimates of surface solar radiation for use in a hydrologic model of the semiarid regions of northwest Mexico and the southwest United States.

The value of calculating daily average cloud cover from the 12 images available from the *GOES-7* satellite series, rather than from the single daily images that might be available from a polar-orbiting satellite, was demonstrated. This study also revealed that, in areas that include complex mixtures of ocean and land, cloud images that are analyzed at low spatial resolution (as in the ISCCP dataset) might be prone to overestimating the cloud cover by a factor of 2.

*Acknowledgments.* Primary support for the preparation of this paper came from NASA Project NAG8-1531. Additional support came from NASA-EOS Interdisciplinary Science Project OSS A-A/88. The *GOES-7* and ground data were gathered as part of research supported by the European Community under Contracts CI1*-CT91-0900 and CI1*-CT94-0059. In addition, J. Garatuza received support under a CONACYT Fellowship. The work of R. T. Pinker was supported under NOAA Grant NA86GOP202 and NASA Grant NAG56667. We are happy to acknowledge the NASA Langley DAAC for allowing access to the ISCCP data. The editorial assistance provided by Corrie Thies is much appreciated.

TABLE 4. Monthly mean cloudiness for Jun and Jul 1994. (a) The cloudiness derived using high-resolution data. (b) The cloudiness derived from the sampled data that simulate the ISCCP intermittent sampling. In both cases the same procedure was used to estimate cloud amount.

| Month | Site 1 | Site 2 | Site 3 | Site 4 | Site 5 | Site 6 |
|---|---|---|---|---|---|---|
| Jun 1994 (a) | 10.2 | 35.2 | 27.5 | 12.3 | 8.8 | 18.8 |
| Jun 1994 (b) | 16.9 | 37.8 | 34.1 | 17.1 | 26.3 | 24.8 |
| Jul 1994 (a) | 12.8 | 22.4 | 22.1 | 15.4 | 17.3 | 17.2 |
| Jul 1994 (b) | 19.9 | 27.2 | 27.8 | 19.7 | 30.9 | 26.3 |

## REFERENCES

Cess, R. D., and Coauthors, 1990: Intercomparison and interpretation of climate feedback processes in 19 atmospheric general circulation models. *J. Geophys. Res.,* **95,** 16 601–16 615.

Cotton, W. R., and R. A. Anthes, 1989: *Storm and Cloud Dynamics.* International Geophysics Series, Vol. 44, Academic Press, 883 pp.

Douglas, M. W., R. A. Maddox, K. Howard, and S. Reyes, 1993: The Mexican monsoon. *J. Climate,* **6,** 1665–1677.

Gleckler, P. J., and Coauthors, 1995: Cloud-radiative effects on implied oceanic energy transports as simulated by atmospheric general circulation models. *Geophys. Res. Lett.,* **22,** 791–794.

Harrison, E. F., P. Minnis, B. R. Barkstrom, V. Ramanathan, R. D. Cess, and G. G. Gibson, 1990: Seasonal variation of cloud radiative forcing derived from the Earth Radiation Budget Experiment. *J. Geophys. Res.,* **95,** 18 687–18 703.

House, F. B., A. Gruber, G. E. Hunt, and A. T. Mecherikunnel, 1986: History of satellite missions and measurements of the Earth Radiation Budget (1957–1984). *Rev. Geophys.,* **24,** 357–378.

Iqbal, M., 1983: *An Introduction to Solar Radiation.* Academic Press, 390 pp.

Kandel, R., and Y. Fouquart, 1992: The Earth Radiation Budget. *Recherche,* **23** (241), 316–324.

King, M. D., and Coauthors, 1996: Airborne scanning spectrometer for remote sensing of cloud, aerosol, water vapor, and surface properties. *J. Atmos. Oceanic Technol.,* **13,** 777–794.

Lagouarde, J. P., 1991: Use of NOAA AVHRR data combined with an agrometeorological model for evaporation mapping. *Int. J. Remote Sens.,* **12,** 1853–1864.

Leese, J. A., 1994: Implementation plan for the GEWEX Continental Scale International Project (GCIP). Vol. 3: Strategy plan for data management. International GEWEX Project Office Publication Series 9, 49 pp. [Available from IGPO, Silver Spring, MD 20910.]

——, 1997: Major activities plan for 1998, 1999 and outlook for 2000 for the GEWEX Continental-scale International Project (GCIP). International GEWEX Project Office Publication Series 26, 77 pp. [Available from IGPO, Silver Spring, MD 20910.]

Lin, B., B. Wielicki, P. Minnis, and W. Rossow, 1998a: Estimation of water cloud properties from satellite microwave, infrared and visible measurements in oceanic environments. Part 1: Microwave brightness temperature simulations. *J. Geophys. Res.,* **103** (D4), 3873–3886.

——, P. Minnis, B. Wielicki, D. R. Doelling, R. Palikonda, D. F. Young, and T. Uttal, 1998b: Estimation of water cloud properties from satellite microwave, infrared and visible measurements in oceanic environments. Part 2: Results. *J. Geophys. Res.,* **103** (D4), 3887–3905.

Minnis, P., and W. L. Smith, 1998: Cloud and radiative fields derived

from *GOES-8* during SUCCESS and the ARM-UAV spring 1996 flight series. *Geophys. Res. Lett.*, **25,** 1113–1116.

——, P. W. Heck, and D. F. Young, 1993: Inference of cirrus cloud properties using satellite-observed visible and infrared radiances. Part II: Verification of theoretical cirrus radiative properties. *J. Atmos. Sci.,* **50,** 1305–1322.

Pexioto, J. P., and A. H. Oort, 1992: *Physics of Climate.* American Institute of Physics, 520 pp.

Pinker, R. T., and I. Laszlo, 1992: Modeling surface solar irradiance for satellite applications on a global scale. *J. Appl. Meteor.*, **31,** 194–212.

Pruppacher, H. R., and D. J. Klett, 1980: *Microphysics of Clouds and Precipitation.* D. Reidel, 714 pp.

Reynolds, D. W., and T. H. Vonder Haar, 1977: A bi-spectral method for cloud parameter determination. *Mon. Wea. Rev.*, **105,** 446–457.

Rossow, W. B., and R. A. Schiffer, 1991: ISCCP cloud data products. *Bull. Amer. Meteor. Soc.,* **72,** 2–20.

——, and L. C. Garder, 1993: Cloud detection using satellite measurements of infrared and visible radiances for ISCCP. *J. Climate,* **6,** 2341–2369.

——, C. L. Brest, and L. C. Garder, 1989a: Global seasonal surface variations from satellite radiance measurements. *J. Climate,* **2,** 214–247.

——, L. C. Garder, and A. A. Lacis, 1989b: Global seasonal surface variations from satellite radiance measurements. Part I: Sensitivity of analysis. *J. Climate,* **2,** 419–458.

Schiffer, R. A., and W. B. Rossow, 1983: The International Satellite Cloud Climatology Project (ISCCP): The first project of the World Climate Research Program. *Bull. Amer. Meteor. Soc.*, **64,** 779–784.

Seguin, B., and Itier, 1983: Using midday surface temperature to estimate daily evaporation from satellite thermal IR data. *Int. J. Remote Sens.*, **4,** 371–383.

Sèze, G., and W. B. Rossow, 1991: Time-cumulated visible and infrared radiance histograms used as description of surface and cloud variations. *Int. J. Remote Sens.*, **12,** 877–920.

Short, D. A., and R. F. Cahalan, 1983: Interannual variability of climatic noise in satellite-observed outgoing longwave radiation. *Mon. Wea. Rev.,* **111,** 572–577.

Shuttleworth, W. J., 1993: Evaporation. *Handbook of Hydrology,* D. R. Maidment, Ed., McGraw-Hill, 4.1–4.53.

Stowe, L. L., C. G. Wellemeyer, T. F. Eck, H. Y. M. Yeh, and the NIMBUS-7 Cloud Data Processing Team, 1988: NIMBUS-7 global cloud climatology. Part I: Algorithms and validation. *J. Climate*, **1,** 445–470.

Sunada, K., S. Sorooshian, and L. W. Gay, 1990: A basic study on estimation of regional evapotranspiration using remotely sensed data. *J. Hydrosci. Hydraul. Eng.*, **7,** 27–38.

Tarpley, J. D., R. T. Pinker, and I. Laszlo, 1996: Experimental GOES shortwave radiation budget for GCIP. *Proc. Second Int. Sci. Conf. on the Global Energy and Water Cycle*, Washington, DC, 248–285.

Warren, S. G., C. J. Hahn, J. London, R. M. Chervin, and R. L. Jenne, 1986: Global distribution of total cloud and cloud type amounts over the ocean. NCAR Tech. Note TN-317+STR/DOE, Tech. Rep. ER-0406, 42 pp. + 170 maps. [NTIS DE90-00-3187.]

Whitlock, C. H., and Coauthors, 1990: AVHRR and VISSR satellite instrumentation calibration for both cirrus and marine stratocumulus IFO periods. FIRE Science Report 1988, NASA CP-3083, 141–145.

Wielicki, B. A., and L. Parker, 1992: On the determination of cloud cover from satellite sensors: The effect of sensor spatial resolution. *J. Geophys. Res.,* **97,** 12 799–12 823.

——, R. D. Cess, M. D. King, D. A. Randall, and E. F. Harrison, 1995: Mission to Planet Earth: Role of clouds and radiation in climate. *Bull. Amer. Meteor. Soc.,* **76,** 2125–2153.

Wylie, D. P., and W. P. Menzel, 1989: Two years of cloud cover statistics using VAS. *J. Climate,* **2,** 280–392.